



HAL
open science

Spin transport in multilayer graphene away from the charge neutrality point

Xin He, Yan Wen, Chenhui Zhang, Peng Li, Dongxing Zheng, Aitian Chen, Aurelien Manchon, Xixiang Zhang

► **To cite this version:**

Xin He, Yan Wen, Chenhui Zhang, Peng Li, Dongxing Zheng, et al.. Spin transport in multilayer graphene away from the charge neutrality point. *Carbon*, 2020, 172, pp.474-479. 10.1016/j.carbon.2020.10.050 . hal-03034847

HAL Id: hal-03034847

<https://hal.science/hal-03034847>

Submitted on 1 Dec 2020

HAL is a multi-disciplinary open access archive for the deposit and dissemination of scientific research documents, whether they are published or not. The documents may come from teaching and research institutions in France or abroad, or from public or private research centers.

L'archive ouverte pluridisciplinaire **HAL**, est destinée au dépôt et à la diffusion de documents scientifiques de niveau recherche, publiés ou non, émanant des établissements d'enseignement et de recherche français ou étrangers, des laboratoires publics ou privés.

1 **Spin transport in multilayer graphene away from the charge**
2 **neutrality point**

3

4 Xin He^a, Yan Wen^a, Chenhui Zhang^a, Peng Li^{a,b}, Dongxing Zheng^a, Aitian Chen^a,
5 Aurelien Manchon^a, Xixiang Zhang^{a,*}

6

7 ^aPhysical Science and Engineering Division, King Abdullah University of Science and
8 Technology (KAUST), Thuwal 23955-6900, Saudi Arabia

9 ^bInstitute for Quantum Computing, Department of Electrical and Computer Engineering,
10 University of Waterloo, Waterloo N2L, Canada

11

12

13 **ABSTRACT**

14 Graphene is considered as a promising material in spintronics due to its long spin
15 relaxation time and long spin relaxation length. However, its spin transport properties have been
16 studied at low carrier density only, beyond which much is still unknown. In this study, we
17 explore the spin transport and spin precession properties in multilayer graphene at high carrier
18 density using ionic liquid gating. We find that the spin relaxation time is directly proportional to
19 the momentum relaxation time, indicating that the Elliott-Yafet mechanism still dominates the
20 spin relaxation in multilayer graphene away from the charge neutrality point.

21

22 **Keywords:** Multilayer graphene, Ionic liquid gating, Spin transport, Elliott-Yafet mechanism

23

24 1. Introduction

25 Due to the high charge-carrier mobility [1], weak spin-orbit coupling [2, 3], and
26 efficiently gate-tunable transport properties [4], graphene has become a prospective material for
27 spintronics [5-7]. When the study of spintronics in graphene just rose, the spin-relaxation time
28 and spin-relaxation length were measured to be 170 ps and 2 μm [8], respectively, which are
29 much higher than those in the traditional materials [9], yet much lower than the theoretical
30 predictions [10, 11]. The poor quality of the tunneling layer [12], the polymer residues during the
31 fabrication process [13], and the presence of scattering centers in the substrate [14, 15] are
32 considered to be the main factors that degrade the spin transport properties of graphene.
33 Correspondingly, several measures have been proposed to address these problems, such as the
34 optimized insulating layer which facilitates the tunneling injection [12, 16-18], the hexagonal
35 boron nitride (hBN) layer which serves as a substrate or encapsulating layer to provide a smooth
36 interface with reduced trapped charges [19], and the suspended sample structure to avoid
37 impurity scattering [14, 20, 21]. Thanks to these efforts, the spin-relaxation time and spin-
38 relaxation length of graphene have been improved up to 12.6 ns and 30.5 μm [20], respectively,
39 approaching the theoretical prediction gradually [10, 11]. Alternatively, multilayer graphene was
40 also proposed as a promising strategy to improve the spin transport performance since the outer
41 layers of multilayer graphene can screen the electrical potential of impurities [22, 23]. However,
42 this original study was limited to relatively low carrier density (close to $1.25 \times 10^{13} \text{cm}^{-2}$)
43 because of the low efficiency of the traditional solid gate [23]. Hence, the conclusion that the
44 spin relaxation is mainly due to the Elliott-Yafet mechanism was drawn only in the vicinity of
45 the charge neutrality point [23]. When the Fermi level is shifted away from the charge neutrality
46 point, the energy band structure and thus the electron properties will be quite different.
47 Furthermore, the electron-electron interaction will be weakened due to the high-carrier density
48 induced charge screening, which will influence the momentum relaxation time. Therefore, how
49 spin transport evolves and which mechanism dominates the spin relaxation in the high-carrier-
50 density range of multilayer graphene is yet to be explored.

51 Ionic liquid (IL) gating has been widely used in 2D materials due to its high efficiency in
52 tuning carrier density [24, 25]. It has been central to the exploration of the electronic and optical
53 properties [26-29], for the tuning and realization of voltage-controlled superconductivity [30],

54 and manipulation of the magnetic properties [31]. These studies all prove that IL gating is a
55 mature and reliable technique.

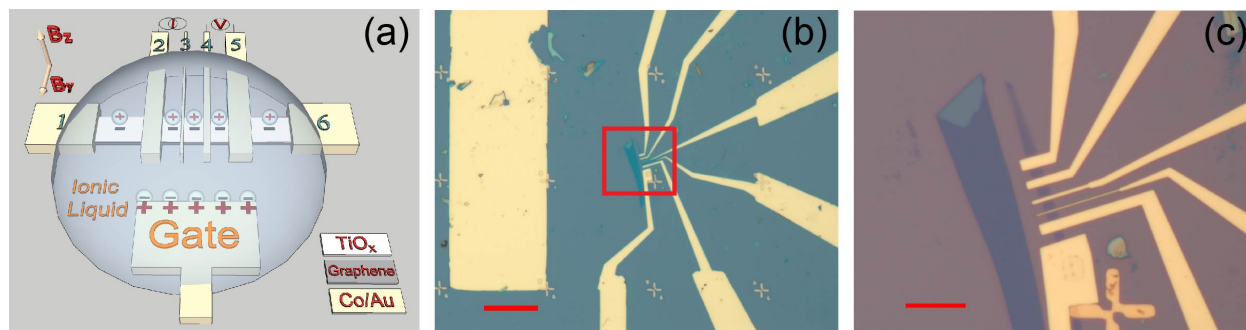
56 In the present study, we explore the spin transport in multilayer graphene by tuning its
57 carrier density using IL gating at 200 K. In a heavily doped multilayer graphene sample, the
58 electron and hole densities reach as high as $4.3 \times 10^{13} \text{ cm}^{-2}$ and $5.7 \times 10^{13} \text{ cm}^{-2}$, respectively.
59 The spin relaxation time and the momentum relaxation time are found to follow a directly
60 proportional relationship, which indicates that the Elliott-Yafet mechanism, rather than the
61 D'yakonov-Perel' mechanism, plays an important role in the high-carrier density range.

62

63 2. Results and analysis

64 The schematic and the optical images of the device for the spin and charge transport
65 measurements are shown in Fig. 1(a-c), while the image with IL on the device can be found in
66 Supplementary Fig. S1. All the electrodes are made of Co/Au (60 nm/ 20 nm). As presented in
67 Fig. 1(a), the outer four electrodes (1, 2, 5, 6) are designed for charge transport measurement
68 using a four-probe configuration, while the inner four electrodes (2, 3, 4, 5) are designed for spin
69 transport measurement; the widths of the central two electrodes (3, 4) are fabricated to be 270
70 and 660 nm, respectively, forming injector and detector electrodes with different coercive fields.
71 The thickness of the multilayer graphene flake was measured to be 4 nm by atomic force
72 microscope. Considering the spacing of adjacent graphene layers is 0.335 nm [23], the layer
73 number of our sample can be estimated to be 12, with an error of about 1 layer. Note that all the
74 measurements in this report were performed at 200 K unless otherwise specified.

75

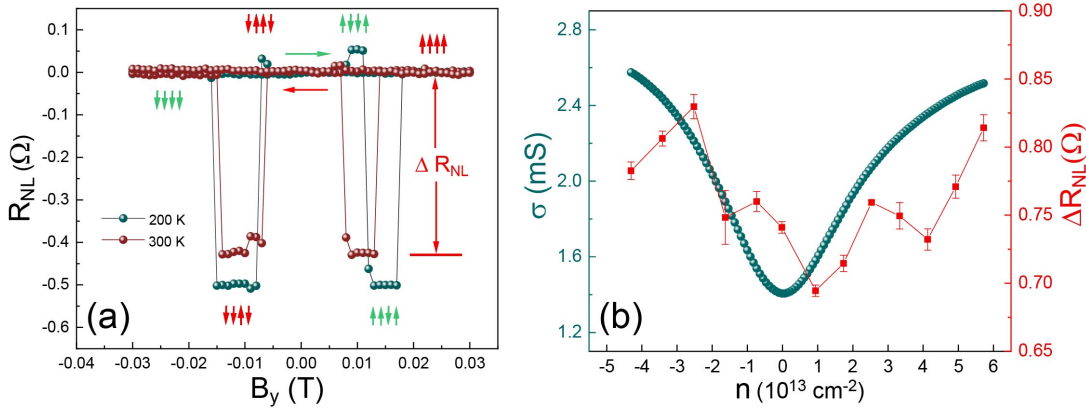


77 **Fig. 1.** (a) Schematic of a nonlocal spin-valve device under IL gating. (b) Optical image of a
78 nonlocal spin-valve device (scale bar: 50 μm). A 12-layer graphene flake is used as the channel.
79 (c) Zoom in on the image framed by the red open box in (b); the scale bar is 10 μm .

80

81 After dropping ionic liquid to cover the whole sample and setting the IL gate floating, the
82 measurements for both spin transport and spin precession were first conducted at 300 K.
83 Subsequently, the system was cooled down quickly to 200 K, the freezing point of ionic liquid
84 [32], so as to avoid chemical reaction between graphene and ionic liquid. The same experiments
85 were also performed at 200 K. As shown in Fig. 1(a), under an in-plane magnetic field (B_y), a
86 current I is injected from electrode 3 (injector) to 2, and then spins accumulate underneath
87 electrode 3 and diffuse along the graphene channel to both sides, inducing a voltage drop V_{NL}
88 between electrode 4 (detector) and 5 and defining the nonlocal resistance $R_{\text{NL}} = V_{\text{NL}}/I$ (spin
89 transport) [8]. The detector probes the chemical potential of the spins impinging from the
90 injector. Therefore, switching the magnetization configuration of the injector and detector from
91 parallel (P) to antiparallel (AP) by sweeping the in-plane magnetic field leads to a sudden
92 decrease of both the nonlocal voltage (ΔV_{NL}) and the nonlocal resistance ($\Delta R_{\text{NL}} = \Delta V_{\text{NL}}/I$), as
93 shown in Fig. 2(a) [8, 33]. The non-local spin valve signal obtained at 200 K is enhanced in
94 comparison to that measured at 300K (Fig. 2(a)), due to the decreased Coulomb scattering in
95 graphene with relatively low carrier mobility, which is consistent with previous reports [34, 35].
96 Applying an out-of-plane magnetic field (B_z), a current I is also injected from electrode 3 to 2,
97 and spins precess as they diffuse from electrode 3 to 4, inducing a voltage drop V_{NL} between
98 electrode 4 and 5 and defining the nonlocal resistance $R_{\text{NL}} = V_{\text{NL}}/I$ as well (spin precession). The
99 non-local Hanle spin precession signals in both 300 K and 200 K are plotted in Supplementary
100 Fig. S2(a) and (b), respectively. At low magnetic fields, the signal weakens because of the
101 reduction of the spin polarization upon increasing the field from zero. When the signal
102 corresponding to the P (AP) configuration decreases (increases) to zero, it indicates that the
103 average angle of the precession reaches 90° [36]. Upon increasing the field further, R_{NL} changes
104 sign and reaches a minimum (maximum) gradually, indicating the reversal of spins (the average
105 precession angle reaches 180°) [36]. However, even though the vertical magnetic field was
106 applied up to 6 T, we could not observe the saturation of R_{NL} that indicates the magnetization of
107 the electrodes has completely rotated out of the plane. This is because the large-resistance

108 background blurs the spin precession signal [37]. Thus, we can only estimate that R_{NL} saturates
 109 at around 1.5 T, at which the slopes of the curves decrease suddenly (Supplementary Fig. S2).

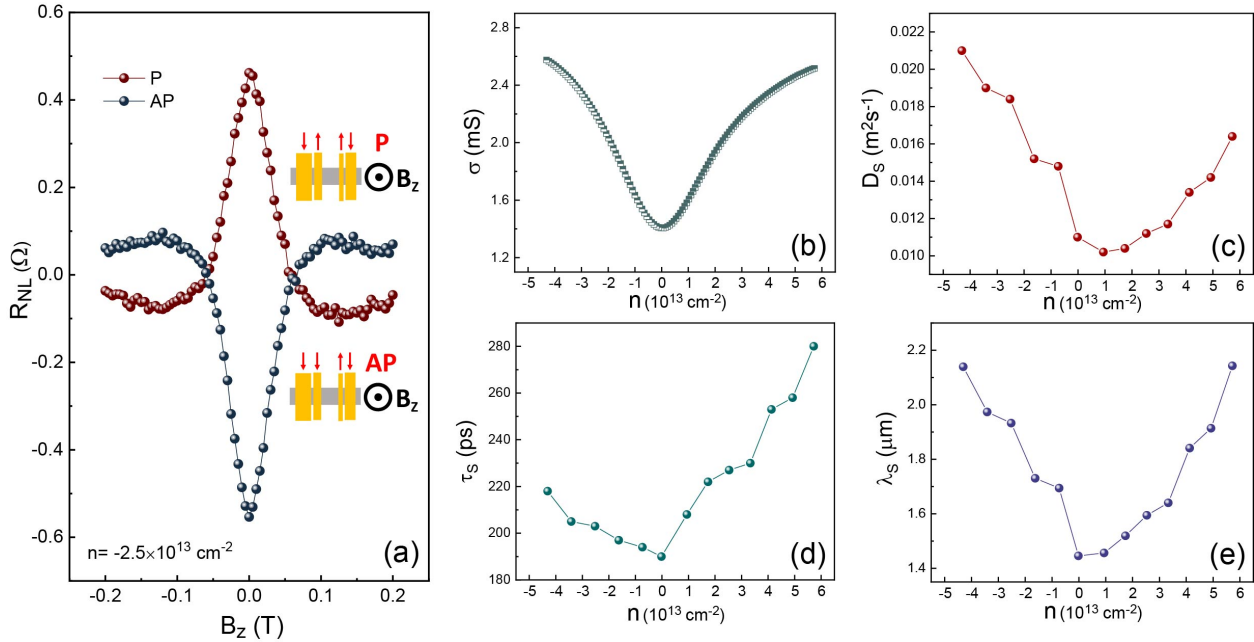


110
 111 **Fig. 2.** (a) Non-local spin valve signal of the 12-layer graphene flake applying an in-plane
 112 magnetic field at 200 K and 300 K. The magnetization configurations of the electrodes are
 113 illustrated by the arrows. The amplitude of the nonlocal resistance is defined as the change of the
 114 nonlocal resistance, ΔR_{NL} . (b) σ (left) and ΔR_{NL} (right) as functions of the carrier density n ,
 115 respectively.

116
 117 To verify the validity of IL gating at 200 K, we performed electronic measurements and
 118 then obtained the standard transfer curve of graphene, with the charge neutrality point located at
 119 $V_{CNP} = 0.59$ V (Fig. S3). This means that IL gating works even at 200 K, suggesting that the
 120 molecules of IL are still mobile at 200 K. Moreover, from Fig. S3, the mobilities (μ) of both
 121 electron and hole are extracted to be $242 \text{ cm}^2/\text{V} \cdot \text{s}$ and $197 \text{ cm}^2/\text{V} \cdot \text{s}$, respectively, by using the
 122 equation, $\mu = \Delta\sigma / (C_{IL}\Delta V_g) = (\Delta(I_{ds}/V_d) \cdot L/W) / (C_{IL}\Delta V_g)$, where σ is the conductivity, I_{ds} is the
 123 drain-source current, V_d is the drain-source voltage, V_g is the gate voltage, C_{IL} is the capacitance
 124 per unit area of IL, L and W are the channel length and width, respectively [38]. C_{IL} is obtained
 125 to be $2.86 \text{ } \mu\text{F}/\text{cm}^2$ and $2.55 \text{ } \mu\text{F}/\text{cm}^2$ for the electron and hole, respectively (Supplementary Note
 126 1), much lower than the values reported previously [26, 39]. There are two factors leading to the
 127 small C_{IL} : the extra TiO_x layer and the screening effect in graphene. First, the inserted TiO_x
 128 layer (about 1 nm thick) increases the effective dielectric thickness of the geometrical
 129 capacitance C_g , which is defined by $C_g = \epsilon_{IL}\epsilon_0/d$, where ϵ_{IL} is the relative permittivity of ionic
 130 liquid, ϵ_0 is the vacuum permittivity, and d is the dielectric thickness [40]. Second, the charges
 131 distributed in the first 3 or 4 layers screen the electric field and quench its penetration, and then

132 C_g saturates to a constant as the layer number is larger than 4 [40]. In Fig. 2(b), the IL gate
 133 voltage is transformed to the carrier concentration N by using the formula, $N = C_{IL} \frac{(V_g - V_{CNP})}{e}$,
 134 where $e < 0$ is the elementary charge [32, 41]. Then the highest electron (hole) density can be
 135 calculated to be $4.3 \times 10^{13} \text{ cm}^{-2}$ ($5.7 \times 10^{13} \text{ cm}^{-2}$). Also in Fig. 2(b), the changes of the non-local
 136 resistances were extracted by performing the non-local spin transport at a series of carrier
 137 densities, as a comparison to the carrier density dependence of the conductivity. The relationship
 138 between ΔR_{NL} and σ in Fig. 2(b) follows neither $\Delta R_{NL} \sim \sigma$ nor $\Delta R_{NL} \sim \frac{1}{\sigma}$, implying that the
 139 electrode contact could be a pinhole type [12]. As discussed in the previous study, the contact
 140 interface mainly affects the polarization of the injected current [23], and the pinhole-type
 141 contacts could also create long spin relaxation time and spin relaxation length [20], thus the
 142 contacts barely influence the spin diffusion and spin relaxation in our study.

143



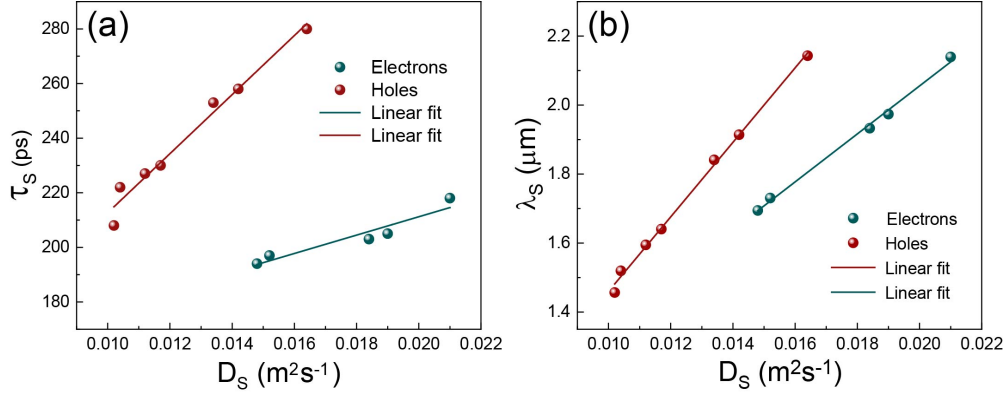
144

145 **Fig. 3.** (a) Nonlocal Hanle spin precession signal of the 12-layer graphene flake at the electron
 146 density of $2.5 \times 10^{13} \text{ cm}^{-2}$, P and AP magnetizations of the central two electrodes are illustrated
 147 in the insets. σ (b), D_s (c), τ_s (d) and λ_s (e) as a function of the carrier density n , respectively.

148

149 The spin precession at different carrier densities is studied applying a perpendicular
 150 magnetic field at 200 K, as shown in Fig. 3. As an example, Fig. 3(a) shows the nonlocal Hanle

151 spin precession signals with both P and AP magnetization of the central electrodes at $V_g = 2$ V,
 152 corresponding to the electron density of $2.5 \times 10^{13} \text{ cm}^{-2}$. Since the magnetic field is applied
 153 perpendicular to the plane, the spins with in-plane orientation begin to precess, following the
 154 Bloch equation for the spin accumulation μ_S , $D_S \nabla^2 \mu_S - \frac{\mu_S}{\tau_S} + \omega_L \times \mu_S = 0$ [23]. The first, second
 155 and third term describes the spin diffusion, spin relaxation, and spin precession, respectively,
 156 with D_S is the spin diffusion coefficient, τ_S is the spin relaxation time, and $\omega_L = \frac{g\mu_B \mathbf{H}}{\hbar}$ is the
 157 Larmor frequency ($g = 2$ is the effective Lande factor, μ_B is the Bohr magneton, and \mathbf{H} is the out-
 158 of-plane magnetic field). Moreover, D_S and τ_S can be extracted by fitting the Hanle precession
 159 signal at each carrier density with the solution of the above Bloch
 160 equation, $R_{NL}^{P(AP)} = (\pm) S_0 \int \frac{1}{\sqrt{4\pi D_S t}} \exp\left(-\frac{L^2}{4D_S t}\right) \cos(\omega_L t) \exp\left(-\frac{t}{\tau_S}\right) dt$ [42] (where $R_{NL}^{P(AP)}$ is the
 161 nonlocal magnetoresistance, \pm sign is for the P (AP) state, S_0 is the amplitude, and L is the
 162 channel length between the central two electrodes), while the spin diffusion length λ_S can be
 163 calculated by $\lambda_S = \sqrt{D_S \tau_S}$ [23]. Note that before fitting the result, the P curve of the Hanle
 164 effect was subtracted from the AP curve (e.g., Fig. 3(a)) to remove the background that is not
 165 related to the spin signal [23]. Therefore, the relationships between σ and n , D_S and n , τ_S and n ,
 166 and λ_S and n are presented in Fig. 3(b-e), respectively. D_S , τ_S , and λ_S all diminish with
 167 decreasing the electron or the hole density, and reach the minimum values in the vicinity of the
 168 charge neutrality point, resembling the relationship between σ and n . Compared with the
 169 previous data obtained using the traditional solid gate in multilayer graphene [23], these
 170 parameters show more significant changes because of the stronger carrier density modulation
 171 induced by the IL gating. The asymmetry of D_S for electrons and holes in Fig. 3(c) may be due to
 172 the nonuniformities in the carrier density [43], while the asymmetry of τ_S in Fig. 3(d) could be
 173 traced to the different impacts of the spin scatterings to the electrons and holes.



174

175 **Fig. 4.** (a) Linear relationship between τ_S and D_S , extracted from Fig. 3(c) and (d). (b) Linear
 176 relationship between λ_S and D_S , extracted from Fig. 3(c) and (e).

177

178 In semiconductors, there are two main mechanisms that contribute to spin relaxation. The
 179 first one is the Elliott-Yafet mechanism, which stems from momentum transfer between spin and
 180 orbital angular momenta during momentum scattering events, resulting in τ_S directly proportional
 181 to τ_P (τ_P is the momentum relaxation time) [43, 44]. The second one is the D'yakonov-Perel'
 182 mechanism, which stems from scattering-induced destructive interference of spins coherently
 183 precessing around the spin-orbit field in the band structure. In this case, τ_S is inversely
 184 proportional to τ_P [43, 44]. Thus, to identify which spin scattering mechanism dominates the spin
 185 relaxation, we need to determine the relationship between τ_S and τ_P . Fig. 4(a) shows the linear
 186 dependence between τ_S and D_S ($\tau_S \propto D_S$), extracted from Fig. 3(c) and (d); while in Fig. 4(b), λ_S
 187 and D_S are also in direct proportion, extracted from Fig. 3(c) and (e). The larger slopes for the
 188 hole regimes indicates the averagely lower spin-flip probability for holes in each scattering [23].
 189 These relationships are consistent with the previous studies in both monolayer and multilayer
 190 graphene [23, 43, 45]. Combing the facts that $D_S \propto D_P$ (D_P is the momentum diffusion
 191 coefficient) [23] and $D_P \propto \tau_P$ [42, 43], we obtain $\tau_S \propto \tau_P$. This indicates that the Elliott-Yafet
 192 mechanism still plays a more important role in the spin relaxation process of multilayer graphene
 193 at high carrier density [43, 44]. Moreover, a large perpendicular electric field can lead to a
 194 considerable in-plane Rashba spin-orbit field, which will affect the spin transport properties, i.g.,
 195 the spin relaxation time [37]. In our experiment, the gate voltage up to 3 V is applied, and the
 196 electric field penetrates to the first 3 or 4 layers of graphene. Considering the ionic liquid
 197 molecule (diameter~1 nm) and the TiO_x layer (thickness~1 nm), the electric field reaches around

198 1 V/nm in graphene theoretically. However, we do not see the deviation of the spin relaxation
199 time in Fig. 3(d), which means that the induced spin-orbit field is quite weak, because of the
200 strong screening of the charges to the applied electric field.

201

202 **3. Outlook**

203 Recently, to realize more functions in graphene-based spin devices, the heterostructures
204 such as graphene/topological insulators [46], graphene/magnetic insulator [47], and
205 graphene/Transition metal dichalcogenides [48] have been constructed. These heterostructures
206 combine both the excellent spin properties of graphene and the exotic properties of other
207 materials via proximity effect. Moreover, the nano-graphene based spin device is also drawing
208 more attention [49-52]. Due to the weak tuning capability of the traditional solid gate, the gate
209 voltage that is used to switch on/off the spin current is always as high as several tens of volts. We
210 believe that the IL gate can be used to improve the gating effect in these devices and allow them
211 to work practically at low voltages.

212

213 **4. Conclusion**

214 In conclusion, we provide more insights into the spin dynamics in multilayer graphene
215 and verified that IL gating is a powerful technique investigating spintronics in 2D materials.
216 After applying IL gate, the electron and hole densities in multilayer graphene are increased up to
217 $4.3 \times 10^{13} \text{ cm}^{-2}$ and $5.7 \times 10^{13} \text{ cm}^{-2}$, respectively. The spin relaxation time and the momentum
218 relaxation time are found to follow a directly proportional relationship, indicating that the Elliott-
219 Yafet mechanism still dominates the spin relaxation in multilayer graphene at high carrier
220 density.

221

222 **5. Methods**

223 Multilayer graphene samples were exfoliated from natural graphite onto SiO₂/Si (300 nm
224 / 500 μm) substrate. To avoid the extra etching process, the samples which were relatively long
225 and narrow were located by optical microscope (Carl Zeiss Imager.A2 Vario with AxioCam

226 HRc), and then their thicknesses were confirmed by atomic force microscope (Asylum Research
227 MFP-3D) using tapping mode. After that, 0.8 nm Ti was evaporated onto the samples using e-
228 beam evaporator, and then they were exposed in air for 0.5 h to form an oxidation layer (the
229 TiO_x layer not only plays a role of tunneling layer to conquer the conductance mismatch
230 problem but also prevents the sample from reacting with ionic liquid) [53]. Subsequently, six
231 electrodes were fabricated for each sample using e-beam lithography (EBL) and followed e-
232 beam evaporation of Co/Au (60 nm / 20 nm). After the lift-off process, the samples were
233 immersed in chloroform (60 °C, 4 hours) to remove the polymer residues to facilitate the usage of
234 IL, which was (N,N-diethyl-N-methyl-N-(2-methoxyethyl)ammonium
235 Bis(trifluoromethanesulfonyl)imide (DEME-TFSI)) (Kanto Chemical Co., Inc.). With Keithley
236 2636B applying IL-gate voltage, an alternating current of 20 μA at 13 HZ was applied by
237 Keithley 6221 and the voltage was measured by lock-in amplifier SR830 in the spin transport
238 measurements, while the alternating current was changed to 1 μA in the electronic transport
239 measurements. The transfer curves in the supplementary material were measured using the
240 Keithley 4200-SCS semiconductor characterization system.

241

242 **Conflicts of interest**

243 The authors declare no competing financial interests.

244

245 **Acknowledgments**

246 This publication is based on research supported by the King Abdullah University of Science and
247 Technology (KAUST), under Award Nos. OSR-2018-CRG7-3717 and OSR-2017-CRG6-3427.

248

249 **Appendix A. Supplementary data**

250 Supplementary data to this article can be found online at XXXXXXXXXX.

251 **References**

- 252 [1] C.R. Dean, A.F. Young, I. Meric, C. Lee, L. Wang, S. Sorgenfrei, et al., Boron nitride substrates for high-
253 quality graphene electronics, *Nat. Nanotechnol.* 5 (2010) 722-726.
- 254 [2] M. Gmitra, S. Konschuh, C. Ertler, C. Ambrosch-Draxl, J. Fabian, Band-structure topologies of
255 graphene: Spin-orbit coupling effects from first principles, *Phys. Rev. B* 80 (2009) 235431.
- 256 [3] H. Min, J.E. Hill, N.A. Sinitsyn, B.R. Sahu, L. Kleinman, A.H. MacDonald, Intrinsic and Rashba spin-orbit
257 interactions in graphene sheets, *Phys. Rev. B* 74 (2006) 165310.
- 258 [4] F. Schwierz, Graphene transistors, *Nat. Nanotechnol.* 5 (2010) 487-496.
- 259 [5] M.V. Kamalakar, C. Groenvelde, A. Dankert, S.P. Dash, Long distance spin communication in chemical
260 vapour deposited graphene, *Nat. Commun.* 6 (2015) 6766.
- 261 [6] S. Roche, Aring, J. kerman, B. Beschoten, J.C. Charlier, M. Chshiev, et al., Graphene spintronics: the
262 European Flagship perspective, *2d Materials* 2 (2015) 030202.
- 263 [7] D. Khokhriakov, B. Karpiak, A.M. Hoque, S.P. Dash, Two-dimensional spintronic circuit architectures
264 on large scale graphene, *Carbon* 161 (2020) 892-899.
- 265 [8] N. Tombros, C. Jozsa, M. Popinciuc, H.T. Jonkman, B.J. van Wees, Electronic spin transport and spin
266 precession in single graphene layers at room temperature, *Nature* 448 (2007) 571-574.
- 267 [9] J. Sinova, S.O. Valenzuela, J. Wunderlich, C.H. Back, T. Jungwirth, Spin Hall effects, *Rev. Mod. Phys.* 87
268 (2015) 1213-1259.
- 269 [10] D. Huertas-Hernando, F. Guinea, A. Brataas, Spin-orbit-mediated spin relaxation in graphene, *Phys.*
270 *Rev. Lett.* 103 (2009) 146801.
- 271 [11] D. Pesin, A.H. MacDonald, Spintronics and pseudospintronics in graphene and topological insulators,
272 *Nat. Mater.* 11 (2012) 409-416.
- 273 [12] W. Han, K. Pi, K.M. McCreary, Y. Li, J.J.I. Wong, A.G. Swartz, et al., Tunneling spin injection into
274 single layer graphene, *Phys. Rev. Lett.* 105 (2010) 167202.
- 275 [13] A. Avsar, I.J. Vera-Marun, J.Y. Tan, G.K.W. Koon, K. Watanabe, T. Taniguchi, et al., Electronic spin
276 transport in dual-gated bilayer graphene, *NPG Asia Mater.* 8 (2016) e274.
- 277 [14] M.H.D. Guimaraes, A. Veligura, P.J. Zomer, T. Maassen, I.J. Vera-Marun, N. Tombros, et al., Spin
278 transport in high-quality suspended graphene devices, *Nano Lett.* 12 (2012) 3512-3517.
- 279 [15] P.J. Zomer, M.H.D. Guimaraes, N. Tombros, B.J. van Wees, Long-distance spin transport in high-
280 mobility graphene on hexagonal boron nitride, *Phys. Rev. B* 86 (2012) 161416(R).
- 281 [16] M.V. Kamalakar, A. Dankert, J. Bergsten, T. Ive, S.P. Dash, Enhanced tunnel spin injection into
282 graphene using chemical vapor deposited hexagonal boron nitride, *Sci Rep* 4 (2014) 6146.
- 283 [17] S. Singh, J. Katoch, J.S. Xu, C. Tan, T.C. Zhu, W. Amamou, et al., Nanosecond spin relaxation times in
284 single layer graphene spin valves with hexagonal boron nitride tunnel barriers, *Appl. Phys. Lett.* 109
285 (2016) 122411.
- 286 [18] M.V. Kamalakar, A. Dankert, P.J. Kelly, S.P. Dash, Inversion of Spin Signal and Spin Filtering in
287 Ferromagnet vertical bar Hexagonal Boron Nitride-Graphene van der Waals Heterostructures, *Sci Rep* 6
288 (2016) 21168.
- 289 [19] M. Gurram, S. Omar, B.J. van Wees, Electrical spin injection, transport, and detection in graphene-
290 hexagonal boron nitride van der Waals heterostructures: progress and perspectives, *2D Materials* 5
291 (2018) 032004.
- 292 [20] M. Droger, C. Franzen, F. Volmer, T. Pohlmann, L. Banszerus, M. Wolter, et al., Spin lifetimes
293 exceeding 12 ns in graphene nonlocal spin valve devices, *Nano Lett.* 16 (2016) 3533-3539.
- 294 [21] M. Droger, F. Volmer, M. Wolter, B. Terres, K. Watanabe, T. Taniguchi, et al., Nanosecond spin
295 lifetimes in single- and few-layer graphene-hBN heterostructures at room temperature, *Nano Lett.* 14
296 (2014) 6050-6055.

297 [22] L. Li, I. Lee, D. Lim, S. Rathi, M. Kang, T. Uemura, et al., Spin diffusion and non-local spin-valve effect
298 in an exfoliated multilayer graphene with a Co electrode, *Nanotechnology* 27 (2016) 335201.
299 [23] T. Maassen, F.K. Dejene, M.H.D. Guimaraes, C. Jozsa, B.J. van Wees, Comparison between charge
300 and spin transport in few-layer graphene, *Phys. Rev. B* 83 (2011) 115410.
301 [24] H.W. Du, X. Lin, Z.M. Xu, D.W. Chu, Electric double-layer transistors: a review of recent progress, *J.*
302 *Mater. Sci.* 50 (2015) 5641-5673.
303 [25] T. Fujimoto, K. Awaga, Electric-double-layer field-effect transistors with ionic liquids, *Phys. Chem.*
304 *Chem. Phys.* 15 (2013) 8983-9006.
305 [26] J.T. Ye, M.F. Craciun, M. Koshino, S. Russo, S. Inoue, H.T. Yuan, et al., Accessing the transport
306 properties of graphene and its multilayers at high carrier density, *Proc. Natl. Acad. Sci. U. S. A.* 108 (2011)
307 13002-13006.
308 [27] D. Braga, I.G. Lezama, H. Berger, A.F. Morpurgo, Quantitative determination of the band gap of WS₂
309 with ambipolar ionic liquid-gated transistors, *Nano Lett.* 12 (2012) 5218-5223.
310 [28] X. He, N. Tang, L. Gao, J.X. Duan, Y.W. Zhang, F.C. Lu, et al., Formation of p-n-p junction with ionic
311 liquid gate in graphene, *Appl. Phys. Lett.* 104 (2014) 143102.
312 [29] X. He, Z.H. Zhang, C.H. Zhang, Y. Yang, M. Hu, W.K. Ge, et al., Exploration of exciton behavior in
313 atomically thin WS₂ layers by ionic gating, *Appl. Phys. Lett.* 113 (2018) 013104.
314 [30] Y. Saito, T. Nojima, Y. Iwasa, Gate-induced superconductivity in two-dimensional atomic crystals,
315 *Supercond. Sci. Technol.* 29 (2016) 093001.
316 [31] Y.J. Deng, Y.J. Yu, Y.C. Song, J.Z. Zhang, N.Z. Wang, Z.Y. Sun, et al., Gate-tunable room-temperature
317 ferromagnetism in two-dimensional Fe₃GeTe₂, *Nature* 563 (2018) 94-99.
318 [32] M.M. Perera, M.W. Lin, H.J. Chuang, B.P. Chamlagain, C.Y. Wang, X.B. Tan, et al., Improved carrier
319 mobility in few-layer MoS₂ field-effect transistors with ionic-liquid gating, *ACS Nano* 7 (2013) 4449-4458.
320 [33] F.J. Jedema, A.T. Filip, B.J. van Wees, Electrical spin injection and accumulation at room
321 temperature in an all-metal mesoscopic spin valve, *Nature* 410 (2001) 345-348.
322 [34] T. Maassen, J.J. van den Berg, N. Ijbema, F. Fromm, T. Seyller, R. Yakimova, et al., Long spin
323 relaxation times in wafer scale epitaxial graphene on SiC(0001), *Nano Lett.* 12 (2012) 1498-1502.
324 [35] T. Yamaguchi, R. Moriya, S. Masubuchi, K. Iguchi, T. Machida, Spin relaxation in weak localization
325 regime in multilayer graphene spin valves, *Jpn. J. Appl. Phys.* 52 (2013) 040205.
326 [36] F.J. Jedema, H.B. Heersche, A.T. Filip, J.J.A. Baselmans, B.J. van Wees, Electrical detection of spin
327 precession in a metallic mesoscopic spin valve, *Nature* 416 (2002) 713-716.
328 [37] M.H.D. Guimaraes, P.J. Zomer, J. Ingla-Aynes, J.C. Brant, N. Tombros, B.J. van Wees, Controlling spin
329 relaxation in hexagonal BN-encapsulated graphene with a transverse electric field, *Phys. Rev. Lett.* 113
330 (2014) 086602.
331 [38] T. Kim, H. Kirn, S.W. Kwon, Y. Kim, W.K. Park, D.H. Yoon, et al., Large-scale graphene micropatterns
332 via self-assembly-mediated process for flexible device application, *Nano Lett.* 12 (2012) 743-748.
333 [39] Y.J. Zhang, J.T. Ye, Y. Matsushashi, Y. Iwasa, Ambipolar MoS₂ thin flake transistors, *Nano Lett.* 12
334 (2012) 1136-1140.
335 [40] E. Uesugi, H. Goto, R. Eguchi, A. Fujiwara, Y. Kubozono, Electric double-layer capacitance between
336 an ionic liquid and few-layer graphene, *Sci Rep* 3 (2013) 1595.
337 [41] R. Misra, M. McCarthy, A.F. Hebard, Electric field gating with ionic liquids, *Appl. Phys. Lett.* 90 (2007)
338 052905.
339 [42] K. Pi, W. Han, K.M. McCreary, A.G. Swartz, Y. Li, R.K. Kawakami, Manipulation of spin transport in
340 graphene by surface chemical doping, *Phys. Rev. Lett.* 104 (2010) 187201.
341 [43] C. Jozsa, T. Maassen, M. Popinciuc, P.J. Zomer, A. Veligura, H.T. Jonkman, et al., Linear scaling
342 between momentum and spin scattering in graphene, *Phys. Rev. B* 80 (2009) 241403(R).
343 [44] A. Avsar, T.Y. Yang, S. Bae, J. Balakrishnan, F. Volmer, M. Jaiswal, et al., Toward wafer scale
344 fabrication of graphene based spin valve devices, *Nano Lett.* 11 (2011) 2363-2368.

345 [45] W. Han, R.K. Kawakami, Spin relaxation in single-layer and bilayer graphene, Phys. Rev. Lett. 107
346 (2011) 047207.

347 [46] D. Khokhriakov, A.W. Cummings, K. Song, M. Vila, B. Karpiak, A. Dankert, et al., Tailoring emergent
348 spin phenomena in Dirac material heterostructures, Science Advances 4 (2018) eaat9349.

349 [47] B. Karpiak, A.W. Cummings, K. Zollner, M. Vila, D. Khokhriakov, A.M. Hoque, et al., Magnetic
350 proximity in a van der Waals heterostructure of magnetic insulator and graphene, 2d Materials 7 (2020)
351 015026.

352 [48] A. Dankert, S.P. Dash, Electrical gate control of spin current in van der Waals heterostructures at
353 room temperature, Nat. Commun. 8 (2017) 16093.

354 [49] Z.Q. Fan, F. Xie, X.W. Jiang, Z.M. Wei, S.S. Li, Giant decreasing of spin current in a single molecular
355 junction with twisted zigzag graphene nanoribbon electrodes, Carbon 110 (2016) 200-206.

356 [50] Z.Q. Fan, W.Y. Sun, X.W. Jiang, Z.H. Zhang, X.Q. Deng, G.P. Tang, et al., Redox control of magnetic
357 transport properties of a single anthraquinone molecule with different contacted geometries, Carbon
358 113 (2017) 18-25.

359 [51] Z.Q. Fan, W.Y. Sun, Z.H. Zhang, X.Q. Deng, G.P. Tang, H.Q. Xie, Symmetry-dependent spin transport
360 properties of a single phenalenyl or pyrene molecular device, Carbon 122 (2017) 687-693.

361 [52] T. Enoki, M. Kiguchi, Magnetism of Nanographene-Based Microporous Carbon and Its Applications:
362 Interplay of Edge Geometry and Chemistry Details in the Edge State, Physical Review Applied 9 (2018)
363 037001.

364 [53] C. Song, J.H. Miao, F. Li, Y.N. Yan, B. Cui, F. Pan, Anomalous Hall effect in one monolayer cobalt with
365 electrical manipulation, J. Alloy. Compd. 696 (2017) 315-320.

366